

# Dynamic rupture process of the Mw 7.8 Kahramanmaraş earthquake (SE Türkiye): Variable rupture speed and implications for seismic hazard

Zijia Wang<sup>1</sup>, Wenqiang Zhang<sup>2</sup>, Tuncay - Taymaz<sup>3</sup>, Zhongqiu He<sup>1</sup>, Tianhong Xu<sup>1</sup>, and Zhenguo Zhang<sup>1</sup>

<sup>1</sup>Southern University of Science and Technology

<sup>2</sup>McGill University

<sup>3</sup>Istanbul Technical University

July 19, 2023

# **Dynamic rupture process of the 2023 $M_w$ 7.8 Kahramanmaraş earthquake (SE Türkiye): Variable rupture speed and implications for seismic hazard**

**Zijia Wang<sup>1</sup>, Wenqiang Zhang<sup>2</sup>, Tuncay Taymaz<sup>3</sup>, Zhongqiu He<sup>1</sup>, Tianhong Xu<sup>1</sup>,  
Zhenguo Zhang<sup>1,4</sup>**

<sup>1</sup>Department of Earth and Space Sciences, Southern University of Science and Technology, Shenzhen, China.

<sup>2</sup>Department of Earth and Planetary Sciences, McGill University, Montreal, Canada

<sup>3</sup>Department of Geophysical Engineering, The Faculty of Mines, Istanbul Technical University, Maslak, Sarıyer, Istanbul, Türkiye

<sup>4</sup>Guangdong Provincial Key Laboratory of Geophysical High-resolution Imaging Technology, Southern University of Science and Technology, Shenzhen, China

Corresponding author: Zhenguo Zhang ([zhangzg@sustech.edu.cn](mailto:zhangzg@sustech.edu.cn))

## **Key Points:**

- The high initial stress accumulated in the seismic gap leads to the successful triggering of the East Anatolian Fault.
- The change of fault geometry in the southwest segment prevented the sustained supershear rupture.
- The risk of earthquake nucleation on the secondary fault triggering the major fault rupture and the related disaster was highlighted.

**Abstract**

We considered various non-uniformities such as branch faults, rotation of stress field directions, and changes in tectonic environments to simulate the dynamic rupture process of the 6<sup>th</sup> February 2023  $M_w$  7.8 Kahramanmaraş earthquake in SE Türkiye. We utilized near-fault waveform data, GNSS static displacements, and surface rupture to constrain the dynamic model. The results indicate that the high initial stress accumulated in the Kahramanmaraş-Çelikhan seismic gap leads to the successful triggering of the East Anatolian Fault (EAF) and the supershear rupture in the northeast segment. Due to the complexity of fault geometry, the rupture speed along the southeastern segment of the EAF varied repeatedly between supershear and subshear, which contributed to the unexpectedly strong ground motion. Furthermore, the triggering of the EAF reminds us to be aware of the risk of seismic gaps on major faults being triggered by secondary faults, which is crucial to prevent significant disasters.

**Plain Language Summary**

On February 6, 2023, the south-central Türkiye was hit by two major earthquakes with magnitudes of  $M_w$  7.8 and  $M_w$  7.6 respectively. Among them, the complex rupture process and unexpected ground motion of the  $M_w$  7.8 event attracted the attention of seismologists. In this paper, the 3D dynamic rupture process of this mainshock is simulated based on complex multi-fault system and heterogeneous initial stress. And the simulation results are in good agreement with the observations. Our results show that high initial stress is required for the EAF to be triggered. The supershear rupture occurred only in certain fault segments and is unable to sustain itself in a significant area on the fault due to the along-strike variations in

fault geometry and strength. More importantly, the dynamic model suggests that we must be alert to the risk of major fault being triggered by earthquakes on nearby small faults, especially when there are seismic gaps on the major fault.

## 1 Introduction

On 6<sup>th</sup> February 2023, at 01:17:34 UTC, the  $M_w$  7.8 earthquake struck the Nurdağı-Pazarcık region in the Kahramanmaraş-Gaziantep province of south-central Türkiye, near the NW Syria (Melgar et al., 2023). The 2023 SE Türkiye earthquake sequence occurred in a region where a tectonically deforming complex network of faults controlled by the triple junction between the Anatolian, Arabian, and African plates (Figure. 1). The U.S. Geological Survey, National Earthquake Information Center (USGS-NEIC) located the  $M_w$  7.8 hypocenter on a splay fault south of the EAF, with a strike-slip mechanism consistent with the left-lateral motion of the East Anatolian Fault Zone (EAFZ) (Goldberg et al., 2023a, b). The main shock's epicenter and its subsequent aftershocks were consistently located along the EAF and widespread structural damage was reported in a wide region over eleven major cities and the NW Syria. The EAFZ is the major plate boundary that accommodates the westward extrusion of the Anatolia toward the Aegean Sea, and the fault zone has caused destructive earthquakes throughout recorded history (e.g., Ambraseys, 1989; Emre et al., 2018). The 2023 sequence's mainshock  $M_w$  7.8 has been the most significant and destructive earthquake along the EAFZ and surrounding fault segments since the 22 May 1971  $M_s$  6.9 Bingöl, and 24 January 2020  $M_w$  6.7 Doğanyol-Sivrice earthquakes (Taymaz et al., 1991, 2021). To the south of the EAFZ, the left-lateral Dead Sea Fault (DSF) accommodates northward motion of the Arabian Peninsula relative to the African and Eurasian plates (Taymaz et al., 1991; Figure. 1).

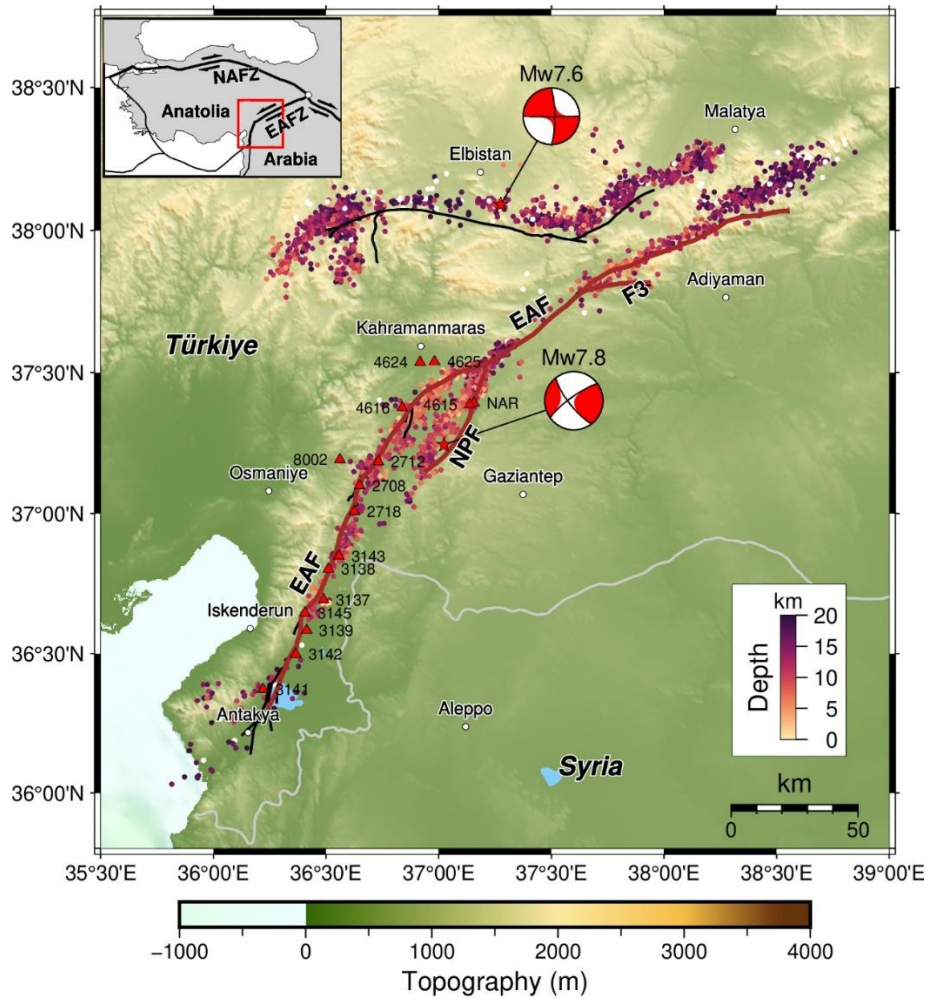


**Figure 1.** Tectonic map of the 2023 SE Türkiye-Syria earthquake doublet and strong-motion stations depicted by red-filled triangles. Two epicenters of  $M_w$  7.8 and  $M_w$  7.6 earthquakes and focal mechanisms from the AFAD are shown as red stars and red beachballs, respectively. Brown lines represents the fault segments used in the dynamic modeling, while black lines show fault traces of mapped surface ruptures from Reitman et al. (2023). The colored-filled circles show the first 11 days of relocated aftershocks (color varying according to the hypocenter depth) from Melgar et al. (2023). Inset illustrates two major tectonic plates (Arabian and Anatolian) and active faults (Emre et al., 2018) and plate boundaries (Bird, 2003), such as East Anatolian Fault Zone (EAFZ) and North Anatolian Fault Zone (NAFZ) (see also Taymaz et al., 1991).

After the 2023 doublet sequence, many preliminary results of finite-fault source inversion based on strong ground motion, near-field geodetic data and/or teleseismic data have been published (Delouis et al., 2023; Mai et al., 2023; Melgar et al., 2023; Goldberg et al., 2023,a, b; Okuwaki et al., 2023; Xu et al., 2023). However, a highly debated controversy exists regarding the presence of a supershear rupture during the  $M_w$  7.8 event. The controversy is multifaceted. Rosakis et al. (2023) analyzed the waveforms of two near-fault stations, concluding that the supershear rupture occurred on the splay fault at a distance of about 19 km from the epicenter. Conversely, some inversion results do not support this conclusion (Delouis et al., 2023; Melgar et al., 2023). Through analyzing the rupture phase, Yao & Yang (2023) determined that the average rupture speed of the southwest section of the EAF is estimated to be  $\sim 3.1$ - $3.4$  km/s. However, this still does not eliminate the possibility of transient supershear. The preliminary dynamic rupture models also remain disputed. The first order model by Gabriel et al. (2023) is subshear, while Abdelmeguid et al. (2023) observe many transient supershear ruptures in the southwest segment and sustained supershear in the northeast segment of the EAF in their 2D simulation. Therefore, to comprehensively understand the rupture process of the 2023 Kahramanmaraş earthquake, it is necessary to conduct detailed data-constrained 3D dynamic simulations.

In this study, we utilize near-fault waveform data, GNSS static horizontal displacement, and surface rupture as constraints to develop a dynamic rupture model for the  $M_w$  7.8 Kahramanmaraş earthquake based on cascading multi-scale network of fault system and heterogeneous initial stress. We thoroughly analyzed the triggering process of the EAF and the rupture speed of our model, followed by a discussion on the implications for the

seismogenic environment and widespread earthquake disaster. Finally, we discuss the earthquake physics and the future improvement for the dynamic model of this earthquake.

## **2 Materials and Methods**

Fault geometry, initial stress, and rock properties control the dynamic rupture process of tectonic faults. However, these data cannot always be measured directly in-situ. In this section, we will discuss the fault model and dynamic parameters adopted based on various previous studies of the EAFZ and introduce the numerical method used for this work.

We construct 3D non-planar fault geometry based on the mapped surface ruptures from Reitman et al. (2023) and earthquake relocation results provided by Melgar et al. (2023). Some smaller fault branches were ignored but we kept the two major ones (Figure 1). These two branches of faults have not been mapped before. Melgar et al. (2023) designated the fault where the rupture was initiated as the Nurdağı-Pazarcık Fault (NPF). In this work, we label another branch fault as the F3 segment (Figure 1). The dip of the EAF is set to  $85^\circ$  trending southeast but bends to  $80^\circ$  trending northwest in northeastmost segment. This dip transition is the same as the fault model of Melgar et al. (2023). The dip of the NPF is set to  $80^\circ$  (trending northwest) based on the earthquake relocation results. The F3 segment shares the same dip and trend as the main portion of the EAF. All fault widths are set to 20 km.

The EAF is located at the intersection of the Arabian, Eurasian, and African plates, resulting in a complex stress state (Taymaz et al., 1991, 2021). Güvercin et al. (2022) studied the stress orientations based on focal mechanisms and found that the orientation varies across different fault segments. In the region that ruptured in the 2023  $M_w$  7.8 event, the direction of

maximum principal compressive stress  $S_H$  is roughly between N169°E and N203°E, with a clockwise trend from southwest to northeast. Early research (Lyberis et al., 1992; Yilmaz et al., 2006) also confirmed the same features. Therefore, after trial-and-error, the  $S_H$  orientation is set as shown in Figure 2a.

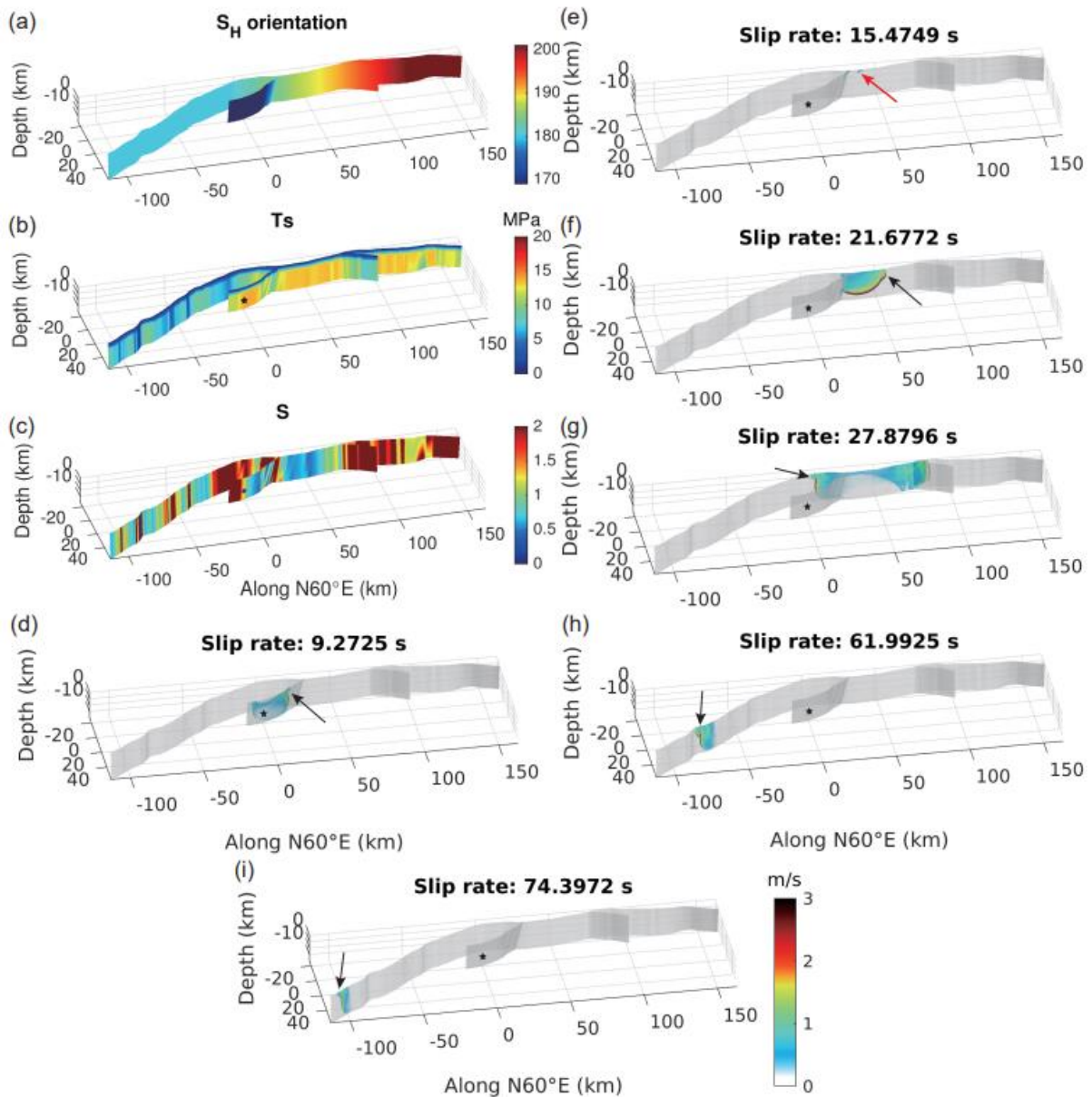


**Figure 2.** Model setting and dynamic rupture results. (a) The orientation of  $S_H$ . (b) Initial shear stress  $T_s$ . (c) The relative fault strength  $S$ . (d)-(i) Key snapshots of the dynamic rupture



process. A shared color bar is illustrated in (i). The black arrows indicate the supershear rupture. The red arrow indicates the dynamic triggering. The black star indicates the epicenter.

Another factor that can constrain the initial stress is the stress shape ratio  $R$ , which is defined as  $R = (S_v - S_H)/(S_h - S_H)$ , where  $S_h$  is the minimum principal stress,  $S_v$  is the vertical stress. Generally, considering lithostatic pressure and pore pressure,  $S_v$  can be described as

$$S_v = (1 - \gamma)\rho gh. \quad (1)$$

Where  $\rho$  is the density of rock,  $g$  is the acceleration of gravity,  $h$  is the depth,  $\gamma$  is the pore-fluid factor, respectively. Therefore, using a lateral pressure coefficient expressed as  $k = S_H/S_v$ , we can obtain

$$S_h = (1 - k + kR)S_v/R. \quad (2)$$

According to the focal mechanism inversion conducted by Yilmaz et al. (2006), the average value of  $R$  in the Kahramanmaraş to Çelikhan segment (KC segment) of the EAF is 0.715. This indicates that the tectonic environment in this region is characterized by transpression. But in the southwest segment of the EAF, the tectonic environment shifts to transtension (Lyberis et al., 1992), we assume  $R = 0.3$  in this region.

After trial-and-error, we set  $\gamma = 0.7$ . To prevent excessive stress drop in the deep part and consider the increased pore pressure along depth (Rice, 1992), the stress only increases to 5 km with depth. The final initial shear stress and the relative fault strength  $S$  (defined as  $(\tau_p - \tau_0)/(\tau_0 - \tau_d)$ , where  $\tau_p$ ,  $\tau_0$  and  $\tau_d$  are the peak shear stress, the initial shear stress and the dynamic friction stress, respectively) are shown in Figure 2b-c. We set the location of the

nucleation zone based on the hypoDD relocations of Melgar et al. (2023). The radius of the nucleation zone is artificially set to 1.8 km. And the shear stress of the nucleation zone is set to a value 0.1% higher than the shear strength to trigger the rupture. The distribution of  $k$  and  $R$  are illustrated in Figure S1.

Here, slip-weakening friction law (Ida, 1972) is applied in our simulation, and also in a recent study by Taymaz et al. (2022). Khalifa et al. (2018) investigated the rock strength of the EAFZ, they found that the rock strength varied from very low to moderate from west to east in the KC segment of the fault. Thus, the friction coefficients are also heterogeneous in the fault plane (Figure S2). The critical slip distance  $D_c$  only varies with depth (Figure S3). The value of  $D_c$  is set to 0.36 m in the depth of 0-15 km and is linearly increased when the depth is larger than 15 km to mimic the brittle-ductile transition in the crust.

In addition, noting that our model setting is very heterogeneous, we explain the necessity of considering stress field rotation and non-uniform friction coefficients in the supplementary materials (see Text S1, Figure S5-S6). A layered seismic velocity structure (Güvercin et al., 2022) is adopted in our dynamic modeling (see Table S1). This model only provides P and S wave velocity  $V_p$  and  $V_s$ , hence we use the empirical formula (Brocher, 2005) to calculate the density  $\rho$  according to  $V_p$ .

In this work, we use an open-source software DRDG3D, which was developed by Zhang et al. (2023) for the dynamic rupture modeling. DRDG3D is based on a nodal discontinuous Galerkin (DG) framework (Hesthaven and Warburton, 2008) with tetrahedral mesh adopted. Due to the flexibility for modeling geometric complex faults, DG methods has been widely used in dynamic rupture modeling of real or scenario earthquakes (Biemiller et

al., 2022; Ramos et al., 2021; Ulrich et al., 2019; Wollherr et al., 2019). DRDG3D adopts an upwind/central mixed flux scheme, which removes numerical artifacts when the near-fault asymmetric unstructured tetrahedral mesh is generated. The numerical scheme of DRDG3D reduces the dependence of mesh quality thereby increasing the efficiency. The DRDG3D has been verified by many benchmark models in the *SCEC/USGS Spontaneous Rupture Code Verification Project* (<https://strike.scec.org/cvws/>, Harris et al, 2009). The accuracy and efficiency of DRDG3D has been analyzed in detail by Zhang et al. (2023).

### 3 Results

The fault element size of our dynamic simulation is 570 m, with the spatial-order-of-accuracy of 3. The time step is 0.0031 s and the total simulation time is 90 s. Figure 2d-i shows some key snapshots of the rupture process. The complete dynamic rupture process can be found in Movie S1. The rupture nucleated at the NPF and generated a supershear rupture at about 9 s (Figure 2d), supporting the preliminary analysis of Rosakis et al. (2023). And then, the EAF was dynamically triggered in the northeast of the junction (Figure 2e). After being triggered, the rupture propagated northeast on the EAF and transitioned to a supershear rupture very quickly (Figure 2f). As the fault strength increased along the strike, the rupture speed returned to subshear (Figure 2g). A few seconds later, the rupture began to propagate southwest. Due to the complex segmented fault geometry, the rupture speed varies frequently (see Figure 2g-i, Figure 3b). The supershear rupture encounters barriers caused by fault geometry changes, making it unsustainable. The final slip distribution of our dynamic model is presented in Figure 3a. The maximum strike-slip displacement exceeds 7 m.

We calculate the rupture speed by the reciprocal of the gradient of the rupture time (Figure 3b), and the rupture time definition threshold is slip rate greater than 0.001 m/s. The overall results of rupture speed are different from Melgar et al. (2023) but are similar to that of Delouis et al. (2023). There may be various reasons for the different results, such as different velocity models or data processing of different research groups. Moreover, Abdelmeguid et al. (2023) analyzed the fault normal and fault parallel components of near-fault stations. They concluded the Station NAR and 3145 showing the characteristics of supershear rupture, which also consistent with our results.

From the  $S$  value and the snapshot of rupture process shown in Figure 2c, we can find that the supershear rupture in the northeast section of the EAF (Figure 2f) may be caused by Burridge-Andrews mechanism, and the supershear rupture in Figure 2g should be induced by free surface. Two supershear ruptures in the southwest section of the EAF (Figure 2h-i) also started from the free surface, but the corresponding  $S$  value is also very low.

The rupture duration for the earthquake simulated in this study is approximately 80 s, and the moment magnitude achieved is  $M_w$  7.8665. Figure 3c compared the moment rate release process of this work, the inversion results of Melgar et al. (2023), Okuwaki et al. (2023), USGS (2023) (for details see Goldberg et al., 2023a, b). All the results show consistency in terms of duration and seismic moment release characteristics, with the maximum peak occurring at 20-30 s and the second peak at 40-50 s. These two peaks correspond to the two periods of maximum energy release for this earthquake.

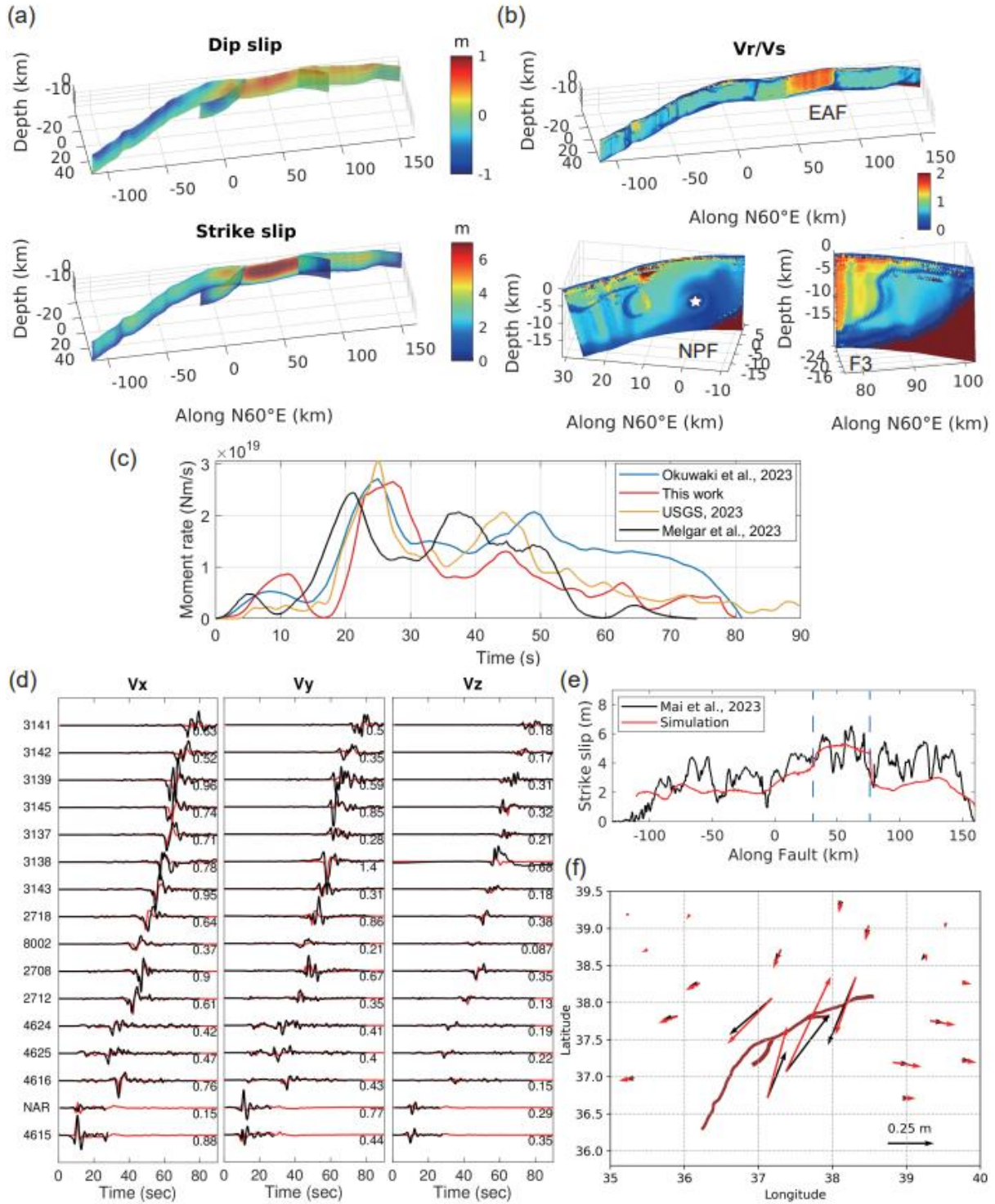


**Figure 3.** (a) Final slip distribution of the dynamic model. (b) The ratio of rupture speed  $V_r$  and  $V_s$ .  $V_r/V_s$  greater than 1 indicates the supershear rupture. The three faults are drawn separately and marked on the figure. There is no rupture in the crimson region except the nucleation zone. The white star indicates the epicenter. (c) Moment rate release comparison.

(d) Comparison of waveforms of near-fault stations. The black line is the observed waveform, and the red line is the synthesized waveform, both of which are filtered to 0.01-0.4 Hz. The station name is marked on the left. The maximum absolute values of each component of the observations (m/s) are listed at the end of each seismogram (see Figure 1 for the location of the stations). (e) Comparison of surface strike-slip displacement. The red line is the simulation result, and the black line is the data provided by Mai et al. (2023). The two blue dashed lines represent the intersections of NPF (left) and F3 (right) with EAF, respectively. (f) Compared with the static horizontal displacement of GNSS. The black arrow is the observed value and the red arrow is the synthetic value.

Figure 3d shows a comparison of the near-fault station waveforms (filtered to 0.01-0.4 Hz). Our results successfully reproduce the primary features of the observations, and the agreement in travel time between our simulation and the observations suggests that the rupture speed in our model is reasonable. Several stations at the most southwest segment of the fault are not well fitted, which may be because we ignore some small branches at the end of the fault and the 3D heterogeneous velocity models are lacking and the relatively uniform dynamic parameters. The triggering and stopping of the rupture on the small branches we ignore will produce strong ground motion, and our layered model cannot well reflect the amplification effect of the sedimentary basin. We noticed that the aforementioned stations are all located near the southwest segment of the EAF. Unfortunately, the near-fault station records in the northeast segment of the EAF were abruptly terminated for unknown reasons, which made the rupture process in the northeast segment less constrained. Nonetheless, we still select 4 stations to compare the relevant waveforms in Figure S4. The stop time of the

recording is very close to the arrival time of the waveforms, leading us to suspect that the cause of station damage is related to the arrival of rupture. Therefore, it is possible and acceptable that a supershear rupture occurred in the northeast segment of the EAF.

The detailed investigation results of surface rupture have not been seen yet, hence the surface strike-slip is compared with the on-fault displacement measured by Mai et al. (2023) based on the satellite data (Liu et al., 2022a; 2022b; Figure 3e). We have captured the first-order characteristics of surface displacement. Notably, the surface displacement on the backward side of the fault intersection has changed suddenly because of the dynamic unclamping. We also calculate the static horizontal displacement based on the triangular elastic half-space dislocation model (Nikkhoo et al., 2015; Meade, 2007) and compare to the observations (Barbot et al., 2023; Figure 3f). The observational and synthetic displacements are a general match. Some mismatches in displacement vectors may be due to the stronger spatial heterogeneity of the actual slip distribution, as well as the lack of consideration of complex medium models in the calculation of the synthesized displacement.

## **4 Discussions**

### *4.1 Implications for seismogenic environment, process of EAF being triggered and earthquake disaster*

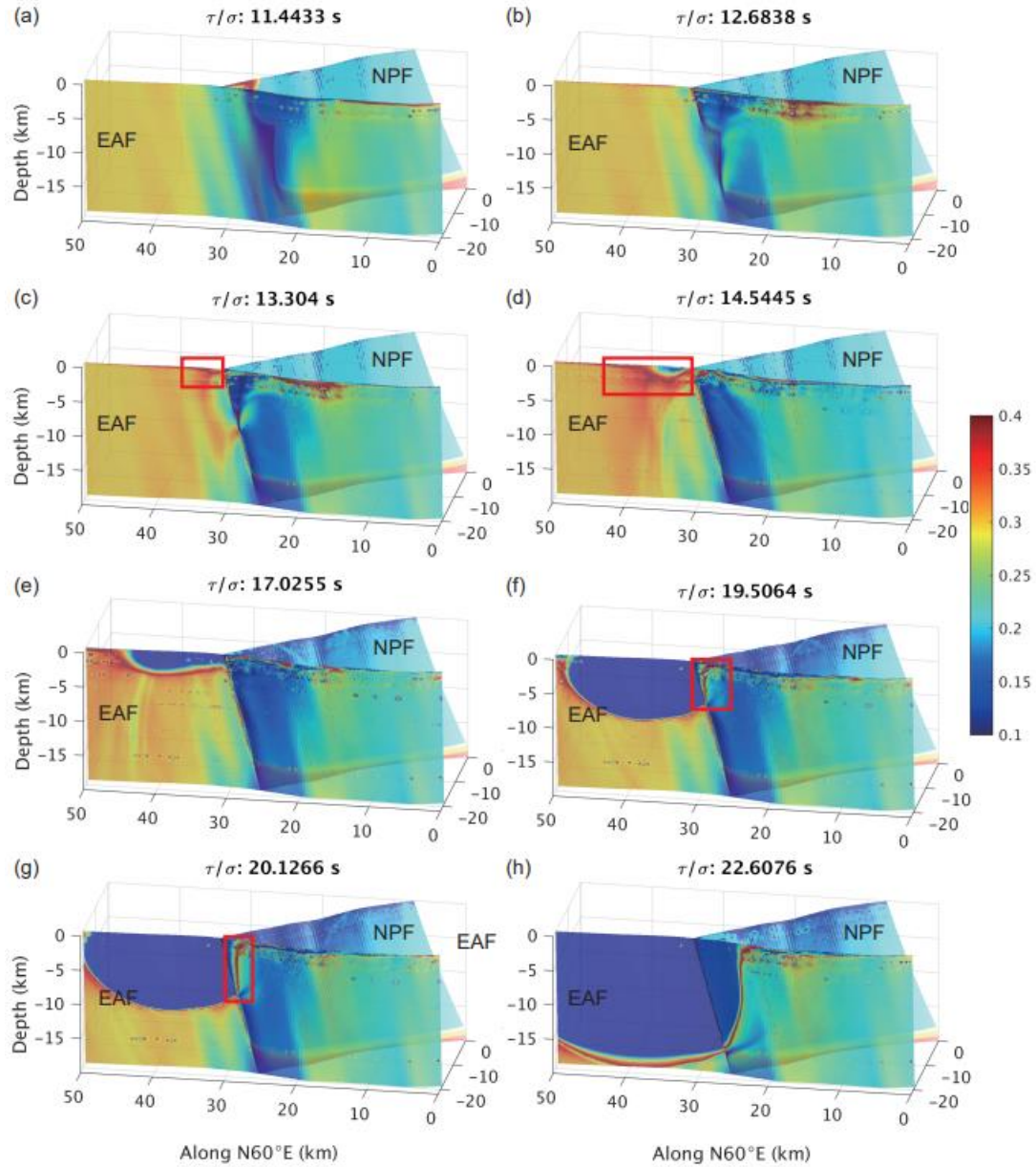
Our dynamic model indicates a high initial stress level in the KC segment of the EAF. Actually, this segment has been identified as a seismic gap with Coulomb stress in an elevated state proposed by Sunbul (2019). Thus, the stress state is consistent with the current seismogenic environment. This plays a crucial role in the triggering process of the EAF.

Because the angle between the NSF and the EAF is about  $30^\circ$ , if the direction of  $S_H$  is close to the optimal stress orientation of one fault, it will be far from the optimal stress orientation of another fault in the range of  $N169^\circ E$ - $N203^\circ E$ . In our model, the  $S_H$  orientation of the fault junction is  $N184^\circ E$ , closer to the optimal stress orientation of the EAF. Therefore, near the fault intersection, the slip rate on the NSF decreases and the dynamic stress decreases, which is not conducive to the rupture propagates to the EAF. However, because the stress in this segment of EAF is high enough, the rupture propagated to the EAF in the northeast of the fault intersection through dynamic triggering. Figure 4 and Movie S2 show the ratio of shear stress and normal stress during the triggering process. More importantly, the high initial stress also leads to the generation of supershear rupture in the northeast segment of the EAF (Figure 3b) and accumulated enough energy to make the rupture propagates backward (Figure 4f-h).

The 2023  $M_w$  7.8 Kahramanmaraş earthquake reminds us of the 2001 Kokoxili earthquake in China and the 2002 Denali earthquake in USA. These two events were also nucleated on secondary faults (Antolik et al., 2004; Eberhart-Phillips et al., 2003). After the rupture propagated to the main fault, a supershear rupture occurred, and the rupture length was also greater than 300km. The difference is that these two earthquakes were unilateral rupture. In addition, the change of rupture speed will produce high-frequency seismic radiation (Vallée et al., 2008), this may also be one of the reasons for the serious damage to Hatay province in southern Türkiye. Therefore, these earthquakes serve as a reminder to remain vigilant as major faults can be triggered by earthquakes nucleated on nearby unrecognized small fault fragments, eventually evolving into giant earthquakes that cause



283 significant damage. This is especially important when there are seismic gaps along the major  
284 fault.



285

286 **Figure 4.** The ratio of shear stress and normal stress during the triggering process. A ratio  
287 equal to  $\mu_s$  (0.4) indicates the position of the rupture front in the EAF. (a) Before the rupture  
288 front reaches the fault intersection. (b) The rupture front reaches the fault intersection. (c-d)  
289 The EAF is triggered, and the red boxes indicate the trigger location. (e) The rupture  
290 propagates northeast and the stress ratio in the backward side is very low indicating it is

difficult to rupture. (f-h) Enough energy is accumulated, and the rupture begins to propagate backward. The red boxes indicate that the rupture is beginning to propagate backward.

#### *4.2 Open questions and future work*

Previous studies have suggested that the EAF is an immature fault (Galović et al., 2020; Melgar et al., 2020; Pousse-Beltran et al., 2020; Taymaz et al., 2021). However, earthquake cycle research shows immature faults are more prone to moderate earthquakes (Thakur & Huang, 2021), this is inconsistent with the situation of the 2023 Kahramanmaraş earthquake. Therefore, does this earthquake manifest that the EAF is going to be mature? If not, why does the rupture length of an immature fault reach 300 km? Thus, there remains further research, such as radiation efficiency should be investigated in detail. Moreover, the 2023 Kahramanmaraş earthquake may be another example of transient supershear ruptures on an immature strike-slip fault like the 2021 Madoi earthquake in China (Cheng et al., 2023).

We didn't consider the topography and the off-fault damage in the dynamic simulation, which may also affect the results. For example, terrain fluctuation is not conducive to the occurrence of free-surface-induced supershear rupture (Zhang et al., 2016). Asymmetric topography along the fault can cause normal stress perturbation of the rupture front near the free surface (Kyriakopoulos et al., 2021). Off-fault plasticity will also consume energy and influence the dynamic rupture process, necessitating a higher initial stress (Gabriel et al., 2013). Future work should also consider the rate and state friction law (Dieterich, 1994; Ruina, 1983), and discuss the impact of thermal pressurization (Rempel & Rice, 2006; Wibberley & Shimamoto, 2005) or flash heating (Goldsby & Tullis, 2011).

## 5 Conclusions

In this work, a data-constrained 3D dynamic rupture model with a complex fault geometry of the 2023 Kahramanmaraş  $M_w$  7.8 earthquake is established. The results show that high initial stress in the KC segment causes the EAF to be triggered. The transient supershear rupture occurs many times, and the change of fault geometry prevents the sustainability of the supershear rupture. Moreover, the triggering process of the NPF to the EAF reminds us that we should pay attention to the seismic activity of the secondary faults adjoining the major fault, and carefully study the risk of the main fault being triggered to prevent the severe casualties from repeating in the future.

## Acknowledgments

The authors declare no competing interests. The authors are grateful to Editor Germán Prieto, and two anonymous reviewers for their constructive comments. We thank Dr. Jihong Liu from King Abdullah University of Science and Technology for providing the on-fault surface displacement data. The authors also thanks Dr. Suli Yao from the Chinese University of Hong Kong, Mathilde Marchandon from the Ludwig-Maximilians-Universität München, and Dr. Lingling Ye from Southern University of Science and Technology for the beneficial discussions. Tuncay Taymaz thanks to Dr. Beyza Taymaz for her phenomenal support during hectic days dealing with global media requests and organizing international scientific collaborations throughout four-weeks of sleepless nights. This work is supported by the National Natural Science Foundation of China (grant no. 42174057), Guangdong Provincial Key Laboratory of Geophysical High-resolution Imaging Technology (2022B1212010002). Tuncay Taymaz thanks to Istanbul Technical University Research Fund (ITU-BAP) and the

Alexander von Humboldt Foundation for providing financial support toward relevant computational resources through the Humboldt-Stiftung follow-up program. This work is supported by Center for Computational Science and Engineering at Southern University of Science and Technology.

## Open Research

The dynamic rupture software DRDG3D is available at <https://github.com/wqseis/drdg3d> (last accessed February 2022). The mapped surface rupture data are from <https://doi.org/10.5066/P985I7U2> (Reitman et al. 2023). The strong ground motion data are downloaded from the Disaster and Emergency Management Authority (AFAD, <https://tadas.afad.gov.tr/event-detail/15499>). The GNSS static horizontal displacement data are available in Table S1 of Barbot et al. (2023, <https://zenodo.org/record/7879743>).

## References

- Abdelmeguid, M., Zhao, C., Yalcinkaya, E., Gazetas, G., Elbanna, A., & Rosakis, A. (2023). Revealing The dynamics of the Feb 6th 2023 M7.8 Kahramanmaraş/Pazarcik Earthquake: near-field records and dynamic rupture modeling, *EarthArXiv*, <https://doi.org/10.31223/X5066R>.
- Antolik, M., Abercrombie, R. E., & Ekström, G. (2004). The 14 November 2001 Kokoxili (Kunlunshan), Tibet, earthquake: rupture transfer through a large extensional step-over, *Bulletin of the Seismological Society of America*, 94(4), 1173-1194, <https://doi.org/10.1785/012003180>.
- Barbot, S., Luo, H., Wang, T., Hamiel, Y., Piatibratova, O., Javed, M. T., et al. (2023). Slip distribution of the February 6, 2023  $M_w$  7.8 and  $M_w$  7.6, Kahramanmaraş, Turkey

earthquake sequence in the East Anatolian Fault Zone, *Seismica*, 2(3),

<https://doi.org/10.26443/seismica.v2i3.502>.

Biemiller, J., Gabriel, A. A., & Ulrich, T. (2022). The Dynamics of Unlikely Slip: 3D

Modeling of Low - Angle Normal Fault Rupture at the Mai'iu Fault, Papua New Guinea,

*Geochemistry, Geophysics, Geosystems*, 23(5), e2021GC010298,

<https://doi.org/10.1029/2021gc010298>.

Bird, P. (2003). An updated digital model of plate boundaries, *Geochemistry Geophysics*

*Geosystems*, 4(3), 1027, <https://doi.org/10.1029/2001GC000252>.

Brocher, T. M. (2005). Empirical Relations between Elastic Wavespeeds and Density in the

Earth's Crust, *Bulletin of the Seismological Society of America*, 95(6), 2081-2092,

<https://doi.org/10.1785/0120050077>.

Cheng, C., Wang, D., Yao, Q., Fang, L., Xu, S., Huang, Z., et al. (2023). The 2021 *M<sub>w</sub>* 7.3

Madoi, China Earthquake: Transient Supershear Ruptures on a Presumed Immature

Strike - Slip Fault, *Journal of Geophysical Research: Solid Earth*, 128(2),

e2022JB024641, <https://doi.org/10.1029/2022jb024641>.

Delouis, B., van den Ende, M., & Ampuero, J.-P. (2023). Kinematic rupture model of the

February 6th 2023 *M<sub>w</sub>* 7.8 Turkey earthquake from a large set of near-source strong

motion records combined by GNSS offsets reveals intermittent supershear rupture,

*Authorea*, <https://doi.org/10.22541/essoar.168286647.71550161/v1>.

Dieterich, J. (1994). A constitutive law for rate of earthquake production and its application

to earthquake clustering, *Journal of Geophysical Research*, 99(B2), 2601-2618,

<https://doi.org/10.1029/93jb02581>.

- Eberhart-Phillips, D., Haeussler, P. J., Freymueller, J. T., Frankel, A. D., Rubin, C. M., Craw, P., et al. (2003). The 2002 Denali fault earthquake, Alaska: A large magnitude, slip-partitioned event, *Science*, 300(5622), 1113-1118, <https://doi.org/10.1126/science.1082703>.
- Emre, Ö., Duman, T. Y., Özalp, S., Şaroğlu, F., Olgun, Ş., Elmacı, H., & Çan T. (2018). Active fault database of Turkey, *Bulletin of Earthquake Engineering*, 16(8), 3229–3275, <https://doi.org/10.1007/s10518-016-0041-2>.
- Gabriel, A.-A., Ulrich, T., Marchandon, M., & Biemiller, J. (2023). Geodetically and seismically informed rapid 3D dynamic rupture modeling of the  $M_w$  7.8 Kahramanmaraş earthquake, in *EGU General Assembly 2023*, edited, Vienna, Austria, <https://doi.org/10.5194/egusphere-egu23-17603>.
- Gabriel, A. A., Ampuero, J. P., Dalguer, L. A., & Mai, P. M. (2013). Source properties of dynamic rupture pulses with off-fault plasticity, *Journal of Geophysical Research: Solid Earth*, 118(8), 4117-4126, <https://doi.org/10.1002/jgrb.50213>.
- Gallovič, F., Zahradník, J., Plicka, V., Sokos, E., Evangelidis, C., Fountoulakis, I., & Turhan, F. (2020). Complex rupture dynamics on an immature fault during the 2020  $M_w$  6.8 Elazığ earthquake, Turkey, *Communications Earth & Environment*, 1(1), <https://doi.org/10.1038/s43247-020-00038-x>.
- Goldberg, D. E., Taymaz, T., Reitman, N. G., Hatem, A. E., Yolsal-Çevikbilen, S., Barnhart, W. D., et al. (2023a). Rapid Characterization of the February 2023 Kahramanmaraş, Türkiye, Earthquake Sequence, *The Seismic Record*. 3(2), 156–167, <https://doi.org/10.1785/0320230009>.

- Goldberg, D. E., Taymaz, T., Yeck, W. L., Barnhart, W. D., Yolsal-Çevikbilen, S., Irmak, T. S., et al. (2023b). Supporting data and models for characterizing the February 2023 Kahramanmaraş, Türkiye, earthquake sequence, U.S. Geol. Surv. Data Release, <https://doi.org/10.5066/P9R6DSVZ>.
- Goldsby, D. L., & Tullis, T. E. (2011). Flash Heating leads to low frictional strength of crustal rocks at earthquake slip rates, *Science*, 6053(14), 216-218, <https://doi.org/10.1126/science.1207902>.
- Güvercin, S. E., Karabulut, H., Konca, A. Ö., Doğan, U., & Ergintav, S. (2022). Active seismotectonics of the East Anatolian Fault, *Geophysical Journal International*, 230(1), 50-69, <https://doi.org/10.1093/gji/ggac045>.
- Harris, R. A., Barall, M., Archuleta, R., Dunham, E., Aagaard, B., Ampuero, J. P., et al. (2009). The SCEC/USGS dynamic earthquake rupture code verification exercise, *Seismological Research Letters*, 80(1), 119–126, <https://doi.org/10.1785/gssrl.80.1.119>.
- Hesthaven, J.S. & Warburton, T., (2008). *Nodal Discontinuous Galerkin Methods: Algorithms, Analysis, and Applications*, (vol. 54). Springer New York. <https://doi.org/10.1007/978-0-387-72067-8>.
- Ida, Y. (1972). Cohesive force across the tip of a longitudinal-shear crack and Griffith's specific surface energy, *Journal of Geophysical Research*, 77(20), 3796-3805, <https://doi.org/10.1029/JB077i020p03796>.
- Khalifa, A., Çakır, Z., Owen, L., & Kaya, Ş. (2018). Morphotectonic analysis of the East Anatolian Fault, Turkey, *Turkish Journal of Earth Sciences*, 27(2), 110-126, <https://doi.org/10.3906/yer-1707-16>.

- Kyriakopoulos, C., Wu, B., and Oglesby D. D. (2021), Asymmetric topography causes normal stress perturbations at the rupture front: The case of the Cajon pass, *Geophysical Research Letters*, 48(20), e2021GL095397, <https://doi.org/10.1029/2021GL095397>.
- Liu, J., Hu, J., Li, Z., Ma, Z., Shi, J., Xu, W., & Sun, Q. (2022a). Three-Dimensional Surface Displacements of the 8 January 2022 Mw6.7 Menyuan Earthquake, China from Sentinel-1 and ALOS-2 SAR Observations. *Remote Sensing*, 14(6), 1404, <https://doi.org/10.3390/rs14061404>.
- Liu, J., Hu, J., Li, Z. Ma, Z., Wu, L., Jiang, W., Feng, G., & Zhu, J. (2022b). Complete three-dimensional coseismic displacements due to the 2021 Maduo earthquake in Qinghai Province, China from Sentinel-1 and ALOS-2 SAR images. *Science China Earth Science*, 65(4), 687–697, <https://doi.org/10.1007/s11430-021-9868-9>.
- Lyberis, N., Yurur, T., Chorowicz, J., Kasapoglu, E., & Gundogdu, N. (1992). The East Anatolian Fault: an oblique collisional belt, *Tectonophysics*, 204(1-2), 1-15, [https://doi.org/10.1016/0040-1951\(92\)90265-8](https://doi.org/10.1016/0040-1951(92)90265-8).
- Mai, P. M., Aspiotis, T., Aquib, T. A., Cano, E. V., Castro-Cruz, D., Espindola-Carmona, A., et al. (2023). The Destructive Earthquake Doublet of 6 February 2023 in South-Central Türkiye and Northwestern Syria: Initial Observations and Analyses, *The Seismic Record*, 3(2), 105-115, <https://doi.org/10.1785/0320230007>.
- Meade, B. J. (2007). Algorithms for the calculation of exact displacements, strains, and stresses for triangular dislocation elements in a uniform elastic half space. *Computers & geosciences*, 33(8), 1064-1075, <https://doi.org/10.1016/j.cageo.2006.12.003>.



- Melgar, D., Ganas, A., Taymaz, T., Valkaniotis, S., Crowell, B. W., Kapetanidis, V., et al., (2020). Rupture kinematics of 2020 January 24 Mw 6.7 Doğanyol-Sivrice, Turkey earthquake on the East Anatolian Fault Zone imaged by space geodesy, *Geophysical Journal International*, 223(2), 862–874, <https://doi.org/10.1093/gji/ggaa345>.
- Melgar, D., Taymaz, T., Ganas, A., Crowell, B., Öcalan, T., Kahraman, M., et al. (2023). Sub- and super-shear ruptures during the 2023  $M_w$  7.8 and  $M_w$  7.6 earthquake doublet in SE Türkiye, *Seismica*, 2(3), 1-10, <https://doi.org/10.26443/seismica.v2i3.387>.
- Nikkhoo, M., & Walter, T. R. (2015). Triangular dislocation: an analytical, artefact-free solution. *Geophysical Journal International*, 201(2), 1119-1141, <https://doi.org/10.1093/gji/ggv035>.
- Okuwaki, R., Yagi, Y., Taymaz, T., & Hicks, S. P. (2023). Multi-scale rupture growth with alternating directions in a complex fault network during the 2023 south-eastern Türkiye and Syria earthquake doublet, *Geophysical Research Letters*, 50(12), e2023GL103480. <https://doi.org/10.1029/2023GL103480>.
- Pousse - Beltran, L., Nissen, E., Bergman, E. A., Cambaz, M. D., Gaudreau, É., Karasözen, E., & Tan, F. (2020). The 2020  $M_w$  6.8 Elazığ (Turkey) Earthquake Reveals Rupture Behavior of the East Anatolian Fault, *Geophysical Research Letters*, 47(13), e2020GL088136, <https://doi.org/10.1029/2020gl088136>.
- Ramos, M. D., Huang, Y., Ulrich, T., Li, D., Gabriel, A. A., & Thomas, A. M. (2021). Assessing Margin-Wide Rupture Behaviors Along the Cascadia Megathrust With 3-D Dynamic Rupture Simulations, *Journal of Geophysical Research: Solid Earth*, 126(7), e2021JB022005, <https://doi.org/10.1029/2021JB022005>.

- Reitman, N.G., Briggs, R.W, Barnhart, W.D., Thompson, J.A., DuRoss, C.B., Hatem, A.E.,  
Gold, R.D., Mejstrik, J.D. (2023). Preliminary fault rupture mapping of the 2023 M7.8  
and M7.5 Türkiye Earthquakes. <https://doi.org/10.5066/P985I7U2>, last accessed March  
2023.
- Rempel, A. W., & Rice, J. R. (2006). Thermal pressurization and onset of melting in fault  
zones, *Journal of Geophysical Research*, 111(B9),  
<https://doi.org/10.1029/2006jb004314>.
- Rice, J. R. (1992). *Fault Stress States, Pore Pressure Distributions, and the Weakness of the  
San Andreas Fault* (Vol. 51, pp. 475–503). Academic Press Ltd.  
[https://doi.org/10.1016/s0074-6142\(08\)62835-1](https://doi.org/10.1016/s0074-6142(08)62835-1).
- Rosakis, A., Abdelmeguid, M., & Elbanna, A. (2023). Evidence of Early Supershear  
Transition in the Feb 6th 2023 *M<sub>w</sub>* 7.8 Kahramanmaraş Turkey Earthquake From Near-  
Field Records, *EarthArXiv*, <https://doi.org/10.31223/X5W95G>.
- Ruina, A. (1983). Slip instability and state variable friction laws, *Journal of Geophysical  
Research*, 88(B12), 10359-10370, <https://doi.org/10.1029/JB088iB12p10359>.
- Sunbul, F. (2019). Time-dependent stress increase along the major faults in eastern Turkey,  
*Journal of Geodynamics*, 126, 23-31, <https://doi.org/10.1016/j.jog.2019.03.001>.
- Taymaz, T., Eyidoğan, H., & Jackson J. A. (1991). Source parameters of large earthquakes in  
the East Anatolian Fault Zone (Turkey), *Geophysical Journal International*, 106(3),  
537–550, <https://doi.org/10.1111/j.1365-246X.1991.tb06328.x>.
- Taymaz, T., Ganas, A., Yolsal-Çevikbilen, S., Vera, F., Eken, T., Erman, C., et al. (2021).  
Source mechanism and rupture process of the 24 January 2020 *M<sub>w</sub>* 6.7 Doğanyol-

Sivrice earthquake obtained from seismo- logical waveform analysis and space geodetic observations on the East Anatolian Fault Zone (Turkey), *Tectonophysics*, 804, 228745, <https://doi.org/10.1016/j.tecto.2021.228745>.

Taymaz, T., Yolsal-Çevikbilen, S., Irmak, T.S., Vera, F., Liu, C., Eken, T., et al. (2022).

Kinematics of the 30 October 2020 Mw 7.0 Néon Karlovásion (Samos) Earthquake in the Eastern Aegean Sea: Implications on Source Characteristics and Dynamic Rupture Simulations, *Tectonophysics*, 826, 229223, <https://doi.org/10.1016/j.tecto.2022.229223>.

Thakur, P., & Huang, Y. (2021). Influence of Fault Zone Maturity on Fully Dynamic Earthquake Cycles, *Geophysical Research Letters*, 48(17), <https://doi.org/10.1029/2021gl094679>.

Ulrich, T., Gabriel, A.-A., Ampuero, J.-P., & Xu, W. (2019). Dynamic viability of the 2016 Mw 7.8 Kaikoura earthquake cascade on weak crustal faults, *Nature Communications*, 10(1), 1213, <https://doi.org/10.1038/s41467-019-09125-w>.

U.S. Geological Survey (2023). Event page for the M 7.8 - Central Turkey, earthquake, <https://earthquake.usgs.gov/earthquakes/eventpage/us6000jllz/>, last accessed March 2023.

Vallée, M., Landès, M., Shapiro, N. M., & Klinger, Y. (2008). The 14 November 2001 Kokoxili (Tibet) earthquake: High-frequency seismic radiation originating from the transitions between sub-Rayleigh and supershear rupture velocity regimes, *Journal of Geophysical Research*, 113(B7), B07305, <https://doi.org/10.1029/2007jb005520>.

- Wibberley, C. A. J., & Shimamoto, T. (2005). Earthquake slip weakening and asperities explained by thermal pressurization, *Nature*, 436(7051), 689-692, <https://doi.org/10.1038/nature03901>.
- Wollherr, S., Gabriel, A. A., & Mai, P. M. (2019). Landers 1992 “Reloaded”: Integrative Dynamic Earthquake Rupture Modeling, *Journal of Geophysical Research: Solid Earth*, 124(7), 6666-6702, <https://doi.org/10.1029/2018jb016355>.
- Xu, L., Mohanna, S., Meng, L., Ji, C., Ampuero, J.-P., Yunjun, Z., et al. (2023). The 2023 *M<sub>w</sub>* 7.8 Kahramanmaraş, Turkey earthquake: a multi-segment rupture in a millennium supercycle, *Research Square*, <https://doi.org/10.21203/rs.3.rs-2747911/v1>.
- Yao, S., & Yang, H. (2023). Rupture phase in near-fault records of the 2023 Turkey *M<sub>w</sub>* 7.8 earthquake, *EarthArXiv*, <https://doi.org/10.31223/X51662>.
- Yilmaz, H., Over, S., & Ozden, S. (2006). Kinematics of the East Anatolian Fault Zone between Türkoğlu (Kahramanmaraş) and Çelikhan (Adiyaman), eastern Turkey, *Earth Planets Space*, 58(11), 1463-1473, <https://doi.org/10.1186/BF03352645>.
- Zhang, W., Liu, Y., & Chen, X. (2023). A Mixed-Flux-Based Nodal Discontinuous Galerkin Method for 3D Dynamic Rupture Modeling, *Journal of Geophysical Research: Solid Earth* 128(6), e2022JB025817. <https://doi.org/10.1029/2022JB025817>.
- Zhang, Z., Xu, J., & Chen, X. (2016). The supershear effect of topography on rupture dynamics, *Geophysical Research Letters*, 43(4), 1457-1463, <https://doi.org/10.1002/2015gl067112>.